Journal of Applied Mathematics and Physics, 2026, 14(2), 648-668
https://www.scirp.org/journal/jamp
ISSN Online: 2327-4379
ISSN Print: 2327-4352

A Coupled Computational Model of Powder Flow and Melt Pool Dynamics in Directed Energy Deposition-Based Metal Additive Manufacturing

Yuduo Wei[1], Dali Ding[2], Yongqi Chen[1], Shaopeng Zheng[1*]

[1]College of Construction Engineering, Jilin University, Changchun, China
[2]School of Energy and Power Engineering, Changchun Institute of Technology, Changchun, China
Email: ydwei23@mails.jlu.edu.cn, dingdali@ccit.edu.cn, yqc@mails.jlu.edu.cn, *zhengsp0428@mails.jlu.edu.cn

How to cite this paper: Wei, Y.D., Ding, D.L., Chen, Y.Q. and Zheng, S.P. (2026) A Coupled Computational Model of Powder Flow and Melt Pool Dynamics in Directed Energy Deposition-Based Metal Additive Manufacturing. *Journal of Applied Mathematics and Physics*, **14**, 648-668.
https://doi.org/10.4236/jamp.2026.142035

Received: January 25, 2026
Accepted: February 10, 2026
Published: February 13, 2026

Abstract

Achieving high-fidelity simulation of the directed energy deposition process requires an integrated approach that captures the critical coupling between powder delivery and melt pool evolution. This paper introduces an innovative coupled computational model that bridges this gap by simultaneously resolving the powder stream dynamics and the melt pool thermo-fluid behavior. The novelty lies in its two-way interaction algorithm, where the powder particles provide mass and enthalpy sink/source terms to the melt pool, while the pool's thermal field and surface morphology influence the particle adhesion and incorporation. Validated with synchronized experimental diagnostics, the model quantitatively links process parameters (e.g., laser power, powder feed rate) to resultant deposit qualities. Key findings include the identification of a nonlinear interaction window where powder flow significantly dampens Marangoni convection, thereby altering solidification patterns. Quantitative comparisons between the simulated bead geometry and experimental metallographic cross-sections demonstrate an exceptional goodness-of-fit, confirming the model's predictive accuracy. Consequently, the proposed model serves as a powerful virtual platform for defect prediction and precise process optimization, marking a significant step toward robust and intelligent metal additive manufacturing.

Keywords

Directed Energy Deposition, Coupled Modeling, Gas-Powder Flow, Melt Pool Dynamics, Process Optimization

1. Introduction

Directed Energy Deposition (DED) stands as a cornerstone technology within metal Additive Manufacturing (AM), enabling the fabrication of fully dense, high-performance metallic components through the synchronized melting of delivered feedstock (typically powder or wire) with a focused high-energy beam (e.g., laser, electron beam) and subsequent layer-by-layer deposition [1]. A typical structure of the laser nozzle used in DED systems is shown in **Figure 1(a)**. Its unique capabilities render it indispensable for applications demanding tailored material properties and geometric complexity, such as component repair and remanufacturing, the production of functionally graded materials, and the rapid prototyping of large-scale structures [2]. However, the DED process is governed by a complex, transient interplay of multi-physics phenomena. As illustrated in the schematic diagram of laser cladding in **Figure 1(b)**, this includes the turbulent gas-powder flow dynamics, the intricate interaction between the energy beam, the powder cloud, and the substrate, and the rapid thermophysical processes within the melt pool—encompassing heat and mass transfer, fluid flow driven by surface tension gradients (Marangoni convection), and rapid solidification [3]. The dynamic coupling between the incoming powder stream and the evolving melt pool directly dictates critical outcomes: deposition geometry, microstructural characteristics, the formation of metallurgical defects (e.g., porosity, lack-of-fusion), and ultimately, the mechanical performance of the built part [4]. Consequently, developing a fundamental, quantitative understanding of this powder-melt pool interaction is a pivotal scientific challenge. Addressing this challenge is essential to transition DED from a largely empirical, trial-and-error-based practice to a predictable and controllable manufacturing technology, thereby unlocking its full potential for high-integrity industrial applications.

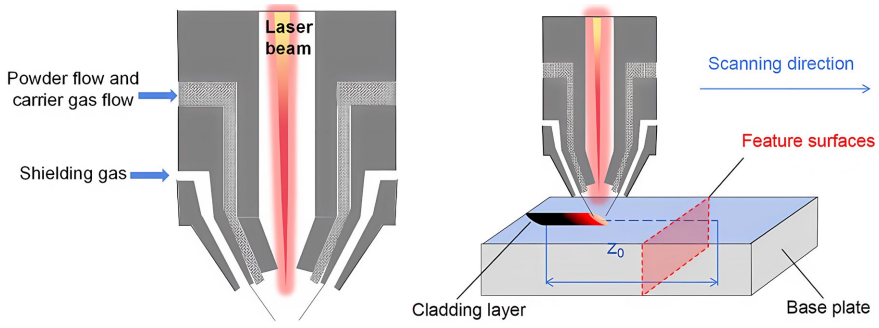

Figure 1. (a) Inside-beam powder feeding nozzle; (b) Laser cladding.

Investigations into powder flow simulation have extensively utilized Discrete Phase Modeling (DPM) or Eulerian-Lagrangian approaches within Computational Fluid Dynamics (CFD) frameworks. These studies have successfully characterized the influence of process parameters—such as carrier gas flow rate, nozzle design, and stand-off distance—on powder stream convergence, focus, and spatial

concentration distribution [5]. For instance, Liu *et al.* [6] provided a detailed analysis of powder concentration fields under different nozzle geometries. While invaluable, these models typically treat the deposition plane as a passive, static boundary, neglecting the dynamic feedback from the actual melt pool's morphology and thermal field on particle impact, heating, melting, and assimilation. Marchais *et al.* [7] utilized discrete element method (DEM) to simulate how particle shape and rigidity affect the spreading mechanism. The research reveals that spherical particles exhibit different flow dynamics compared to irregular ones during the recoating process. Nan *et al.* [8] focused on the numerical modeling of the spreading phase. The authors derive mathematical relationships between blade velocity, gap height, and mass flow rate, offering insights into optimizing recoater design.

For melt pool simulation, researches have predominantly focused on continuum-based approaches, solving coupled Navier-Stokes and energy equations to elucidate the effects of laser parameters, scanning strategy, and thermo-capillary forces on melt pool temperature distribution, fluid flow patterns, and geometry. Kim *et al.* [9] systematically summarized the relationship between process parameters (e.g., continuous wave vs. pulsed lasers) and melt pool characteristics in Selective Laser Melting (SLM), setting a foundation for parameter-optimization studies. Subsequently, research focus expanded to capture the interplay between powder dynamics and melt pool formation. The comprehensive review by Li *et al.* [10] on particle-scale modeling highlighted the integration of the Discrete Element Method (DEM) for powder recoating with Computational Fluid Dynamics (CFD) for melting, providing a state-of-the-art overview of the multi-physics involved in LPBF. Zhang *et al.* [11] developed a model that simultaneously captures gas dynamics, melt pool flow, and powder spattering/entrainment, explicitly revealing how these coupled phenomena lead to defect formation like lack-of-fusion and particle inclusions. This represents a move from descriptive modeling to predictive, mechanism-driven simulation. Li *et al.* [12] constructed three inter-related models—a comprehensive cladding model, a molten pool flow model with user-defined functions, and a coupling model for residual stress analysis—to simulate the integrated thermo-fluid-mechanical behavior. Such work underscores a strong domestic focus on developing practical, high-fidelity simulation tools tailored to complex industrial AM processes.

Recently, some researchers have begun attempts at coupling these two phenomena. Early coupling efforts often adopted "sequential" or "one-way" strategies. For instance, Daniel Weisz-Patrault [13] represented a significant simplification where the complex two-way mass, momentum, and energy exchange is reduced to a one-way thermal input. Reviews of the literature up to this period often noted that studies were "generally segregated with either solely powder flow analysis or melt pool analysis", highlighting the prevalence of these decoupled approaches. Wang *et al.* [14] incorporated two-way coupling mechanisms, where the motion of powder particles (e.g., via DEM) and the fluid dynamics of the melt pool (via

CFD with VOF) are solved concurrently. In such frameworks, particles influence the melt pool through mass and enthalpy transfer upon incorporation, while the melt pool's flow field and thermal gradient exert drag and heating forces on the particles. Wong *et al.* [15] introduced an interface model for integration of molten powder distributive properties into multi-phase simulation, and they proposed new methods to quantify and integrate the effects of molten powder distribution on melt pool characteristics, moving beyond earlier semi-resolved coupling techniques. However, this simplification ignores the real-time, dynamic influence of the formed melt pool on the surrounding flow field (e.g., thermal plume) and particle trajectories above it. It also cannot accurately capture the local disturbances caused by particles entering the melt pool. Although a few studies have introduced more sophisticated two-way coupling frameworks, limitations remain in terms of model completeness, computational efficiency, or thorough experimental validation [16].

To address the identified research gaps, this study aims to develop a high-fidelity, sequentially coupled numerical model to dynamically capture the complex interaction between powder injection and melt pool evolution in the DED process. The structure of this paper is as follows: Section 2 details the development and numerical implementation of the coupled model. Section 3 introduces the experimental setup. Section 4 presents and discusses the simulation and experimental results. Finally, the conclusions are given in Section 5.

2. Computational Methods and Numerical Models

2.1. Gas-Powder Flow Simulation

In the gas-powder two-phase flow model, due to the low volume fraction of powder particles, particle interactions and collisions are reasonably neglected. Based on the multi-phase flow theory, the carrier gas is treated as the continuous phase and solved under turbulent flow conditions, while powder particles are tracked as discrete phases in a Lagrangian framework. The aim of this simulation is to obtain the spatial distribution of the powder before entering the melt pool. This study neglects the in-flight heating and phase change of particles caused by laser irradiation but accounts for the force effects induced by the flow (e.g., drag, inertia, and gravity).

Considering the geometric characteristics of the coaxial nozzle, a 2D axisymmetric model was established. The continuous phase gas is solved using the steady Reynolds-averaged Navier-Stokes (RANS) equations in the cylindrical coordinate system (x,r), where x represents the axial direction and r represents the radial direction. The mass conservation equation is given by:

$$\frac{\partial}{\partial x}\left(\rho_g v_x\right)+\frac{\partial}{\partial r}\left(\rho_g v_r\right)+\frac{\rho_g v_r}{r}=0 \tag{1}$$

The momentum conservation equations for the axial (x) and radial (r) directions are expressed as:

$$\frac{\partial\left(\rho_g v_x v_x\right)}{\partial x}+\frac{1}{r}\frac{\partial\left(r\rho_g v_r v_x\right)}{\partial r}=-\frac{\partial p}{\partial x}+\frac{\partial \tau_{xx}}{\partial x}+\frac{1}{r}\frac{\partial\left(r\tau_{xr}\right)}{\partial r}+F_x \tag{2}$$

$$\frac{\partial\left(\rho_g v_x v_r\right)}{\partial x}+\frac{1}{r}\frac{\partial\left(r\rho_g v_r v_r\right)}{\partial r}=-\frac{\partial p}{\partial r}+\frac{\partial \tau_{xr}}{\partial x}+\frac{1}{r}\frac{\partial\left(r\tau_{rr}\right)}{\partial r}-\frac{\tau_{\theta\theta}}{r}+F_r \tag{3}$$

In the above equations, v_x and v_r denote the axial and radial velocity components of the continuous gas phase, respectively. ρ_g and p represent the gas density and static pressure. The viscous stress tensor components (τ_{xx}, τ_{rr}, τ_{xr}, $\tau_{\theta\theta}$) account for the turbulent transport, where the term $\tau_{\theta\theta}/r$ specifically represents the hoop stress induced by the axisymmetric geometry. Finally, F_x and F_r are the source terms representing the momentum exchange between the gas and the discrete particle phase.

To accurately characterize the turbulent flow behavior within the nozzle and the downstream free shear layer, the Shear Stress Transport (SST) $k-\omega$ turbulence model was employed [17]. This model utilizes a blending function to seamlessly transition from the standard $k-\omega$ formulation in the near-wall region to the $k-\varepsilon$ behavior in the far field, thereby combining the advantages of superior near-wall resolution and free-stream independence. The transport equations for the turbulent kinetic energy (k) and the specific dissipation rate (ω) are expressed as:

$$\frac{\partial}{\partial x_i}\left(\rho_g k u_i\right)=\frac{\partial}{\partial x_j}\left[\left(\mu+\frac{\mu_t}{\sigma_k}\right)\frac{\partial k}{\partial x_j}\right]+\tilde{G}_k-\beta^*\rho_g k\omega \tag{4}$$

$$\frac{\partial}{\partial x_i}\left(\rho_g \omega u_i\right)=\frac{\partial}{\partial x_j}\left[\left(\mu+\frac{\mu_t}{\sigma_\omega}\right)\frac{\partial \omega}{\partial x_j}\right]+\frac{\alpha}{\nu_t}\tilde{G}_k-\beta\rho_g\omega^2+D_\omega \tag{5}$$

where $\tilde{G}_k$ represents the generation of turbulence kinetic energy due to mean velocity gradients. D_ω is the cross-diffusion term arising from the transformation of the $k-\varepsilon$ model, which is essential for the blending strategy. σ_k and σ_ω are the turbulent Prandtl numbers for k and ω, respectively. β^* and β are model constants governing the dissipation of k and ω. The coefficient α is a model parameter related to the production of ω. u_i represents the mean velocity components in the x_i coordinate direction. μ is the molecular dynamic viscosity. In the SST model, the turbulent viscosity μ_t is computed using a shear-stress limiting formulation to prevent the over prediction of eddy viscosity in adverse pressure gradient flows:

$$\mu_t=\frac{\rho_g k}{\omega}\frac{1}{\max\left[\frac{1}{\alpha^*},\frac{SF_2}{a_1\omega}\right]} \tag{6}$$

where S is the strain rate magnitude and F_2 is a blending function that restricts the limiter application to the boundary layer. α^* is the damping coefficient for low-Reynolds number corrections. The model constant a_1 was set to 0.31, and all other constants retained the default values in ANSYS Fluent.

This study employs the FLUENT Discrete Phase Model (DPM) to simulate the motion of powder particles inside and outside the nozzle, using Lagrangian tracking calculations to obtain the spatial distribution pattern of the powder that falls onto the substrate/melt pool region. Due to the low volumetric fraction in the powder delivery process, the dilute-phase assumption is applied. Only the interactions between particles and gas, and particles and wall, are considered, while particle-particle collisions and agglomeration effects are neglected (*i.e.*, the particle collision and four-way coupling modules are not activated). In DPM, the gas continuous phase is treated as an Euler field, while the powder particles are treated as a discrete phase and tracked individually. The particle momentum equation is as follows [18]:

$$m_p \frac{\mathrm{d}u_p}{\mathrm{d}t} = F_D + F_g + F_{other} \tag{7}$$

where m_p denotes unit particle mass, u_p denotes particle velocity; F_D represents the drag term, F_g represents the gravitational term, and F_{other} denotes other optional forces (this study primarily focuses on drag and gravity).

To align with the wall temperature field in the "powder fall into the melt pool criterion," this study enabled the energy equation within the powder distribution model and calculated the convective heat transfer between particles and gas. The particle energy equation can be expressed as:

$$m_p c_p \frac{\mathrm{d}T_p}{\mathrm{d}t} = hA_p\left(T_f - T_p\right) \tag{8}$$

In Equation (8), m_p, c_p, and T_p denote the mass, specific heat capacity, and temperature of the discrete particle, respectively. The term h represents the convective heat transfer coefficient, which governs the heat exchange rate between the particle surface area $A_p = \pi d_p^2$ (d_p is the particle diameter) and the surrounding continuous gas phase (temperature T_f). To close the energy equation, h is evaluated using the semi-empirical nusselt number (Nu_p) correlation proposed by Ranz and Marshall [19]:

$$Nu_p = \frac{hd_p}{k_f} = 2.0 + 0.6Re_p^{1/2}Pr^{1/3} \tag{9}$$

where k_f is the fluid thermal conductivity, Re_p and Pr denote the particle Reynolds number and the Prandtl number [20], respectively.

To characterize the particle-substrate interaction during the DED process, a temperature-dependent "capture-rebound" criterion was implemented [21] in the DPM framework via a User-Defined Function (UDF). Unlike constant-velocity threshold models, this approach incorporates the local phase state (solid, mushy, or liquid) and the temperature-dependent surface tension effects. The liquid fraction, f_l, is first introduced to quantify the phase transition of the substrate surface based on the local temperature T_{wall}:

$$f_l = \begin{cases} 0 & T_{\text{wall}} < T_s \\ \dfrac{T_{\text{wall}} - T_s}{T_l - T_s} & T_s \le T_{\text{wall}} \le T_l \\ 1 & T_{\text{wall}} > T_l \end{cases} \tag{10}$$

where T_s and T_l are the solidus and liquidus temperatures for 316L stainless steel, respectively. These two critical temperatures define the lower and upper bounds of the mushy zone, within which the solid and liquid phases coexist.

Considering that the capture mechanism is governed by the competition between particle inertia and capillary forces, the Weber number (We) is introduced to quantify this relationship. The formula is expressed as:

$$We = \frac{\rho_p v_p^2 d_p}{\sigma} \tag{11}$$

where v_p denotes the impact velocity of the particle perpendicular to the melt pool surface. ρ_p represents the powder particle density. σ refers to the surface tension of the liquid metal. A higher Weber number indicates that inertial forces dominate, facilitating particle entry into the melt pool.

Since the Weber number is inversely proportional to the surface tension σ, the significant variation of surface tension at high temperatures within the melt pool fundamentally alters the capture threshold. Furthermore, within the solid-liquid transition region (mushy zone), the dominant interaction mechanism evolves from elastic-plastic impact on the solid substrate to viscous and capillary damping in the liquid melt. To capture this physical transition, the critical normal velocity, $v_{\text{crit}}(T)$, is formulated by linearly interpolating between the reference thresholds for solid and liquid phases based on the local liquid fraction. This assumes that the surface's energy dissipation capacity scales proportionally with the phase change. Accounting for both this phase evolution and the thermal scaling of surface tension, the expression is given as:

$$v_{\text{crit}}(T) = \left[v_s + f_l (v_l - v_s) \right] \cdot \sqrt{\frac{\sigma(T)}{\sigma_{\text{ref}}}} \tag{12}$$

where f_l is the local liquid fraction; v_s and v_l represent the reference critical velocities for the solid substrate and the fully liquid melt pool, respectively. $\sigma(T)$ is the temperature-dependent surface tension, and σ_{ref} is the reference value at the melting point. Consequently, a particle is captured (trapped) if its incident normal velocity v_n satisfies $v_n \le v_{\text{crit}}(T_{\text{wall}})$; otherwise, it rebounds with a restitution coefficient.

2.2. Molten Pool Dynamics Simulation

Based on the mass flux distribution obtained from the gas-powder flow simulation, a two-dimensional (2D) multi-phase flow model was established to simulate the molten pool evolution. This section gives the governing equations and mass source implementation. The properties of the 316L stainless steel powder and substrate adopted in this numerical model are summarized in **Table 1** [22].

Table 1. Properties of 316L stainless steel.

Parameter	Symbol	Value	Unit
Density	ρ_p	7800	$\mathrm{kg \cdot m^{-1}}$
Specific heat capacity	c_p	0.212T+465.2	$\mathrm{J \cdot kg^{-1} \cdot K^{-1}}$
Thermal conductivity	k	0.01359T+13.77	$\mathrm{W \cdot m^{-1} \cdot K^{-1}}$
Viscosity	μ	1	$\mathrm{Pa \cdot s}$
Solidus temperature	T_s	1722	K
Liquidus temperature	T_l	1790	K
Solidification heat latent	ΔH_f	268,000	$\mathrm{J \cdot kg^{-1}}$
Surface tension at the reference temperature	σ	1.959	$\mathrm{N \cdot m}$
Temperature sensitivity of surface tension	$\frac{\mathrm{d}\sigma}{\mathrm{d}T}$	−0.00043	$\mathrm{N \cdot m \cdot K^{-1}}$
Particle size range	d_p	53 - 105	μm

2.2.1. Governing Equations

The simulation employed the Volume of Fluid (VOF) model [23] coupled with a melting and solidification model. The VOF method determines the free surface by analyzing the fluid volume fraction, α_q, within the computational cells. When the value of α_q for a specific phase range between 0 and 1, it indicates the presence of a fluid interface.

The mass conservation equation governing the VOF model is expressed as:

$$\frac{\partial\left(\alpha_q \rho_q\right)}{\partial t} + \nabla \cdot \left(\alpha_q u \rho_q\right) = S_m \tag{13}$$

where ρ_q is the density of phase q. u is the velocity vector. S_m is the mass source, which simulates synchronous powder feeding by applying a mass source term at the phase interface.

The fluid in the model is assumed to be incompressible laminar flow. The momentum conservation equation is:

$$\frac{\partial}{\partial t}\left(\rho u_i\right) + \frac{\partial}{\partial x_j}\left(\rho u_i u_j\right) = -\frac{\partial p}{\partial x_i} + \frac{\partial \tau_{ij}}{\partial x_j} + \rho g_i + F_i \tag{14}$$

where τ_{ij} represents the stress tensor, g_i is the gravitational body force vector. F_i represents the external body forces, which encompass other model-dependent source terms, such as those for porous media or user-defined sources. Finally, ρ denotes the effective mixture density, defined as the linear summation of the phasic densities weighted by their respective volume fractions:

$$\rho = \sum_{q=1}^{n} \alpha_q \rho_q \tag{15}$$

The energy equation is solved for the mixture phase. To model the laser heating, a volumetric heat source S_h is applied to the mixture energy equation:

$$\frac{\partial(\rho T)}{\partial t}+\nabla\cdot(\rho u T)=\nabla\cdot\left(k_{eff}\nabla T\right)+S_h \tag{16}$$

where T is the temperature and k_{eff} is the effective thermal conductivity, respectively. The heat source S_h is implemented via UDF based on the laser beam profile.

The solidification-melting model in FLUENT employs enthalpy technology, with the enthalpy expression defined as follows:

$$h(T)=\begin{cases}\rho_p c_p T, & T\le T_s\\ h(T_s)+\Delta H_f\dfrac{T-T_s}{T_l-T_s}, & T_s<T<T_l\\ h(T_l)+\rho_p c_p(T-T_l), & T\ge T_l\end{cases} \tag{17}$$

where ΔH_f represents the latent heat of fusion.

This study employs a coaxial powder-feeding laser cladding nozzle. An incident solid laser beam is transformed into a hollow annular beam by a conical lens and an annular focusing lens. When the laser focal plane is located above the cladding surface, an annular hollow spot is formed on the surface. According to [24], the energy density distribution of the hollow laser source is expressed as:

$$q(x,t)=\frac{\eta\cdot 2P}{\pi\left(R_0^2+2R_0 z\cot\varphi\right)}\exp\left\{-\frac{2\left[\sqrt{(x_0-v_s t)^2+x^2}-\left(z\cot\varphi+\xi R_0\right)\right]^2}{R_0^2}\right\} \tag{18}$$

where P is the laser power; η is the laser absorptivity; R_0 is the outer radius of the laser beam at the focal plane; φ denotes the inclination angle of the hollow laser beam relative to the horizontal direction; ξ is the energy-peak position coefficient; z is the defocusing amount; v_s is the scanning speed; and t is the simulation time.

2.2.2. Mass Source Implementation Based on Particle Statistics

To bridge the macro-scale gas-powder flow and the mesoscale molten pool dynamics, a statistical mapping strategy was developed to quantify the spatial distribution of powder particles arriving at the substrate. Based on the discrete trajectory data obtained from the DPM simulation, the particle landing positions were statistically analyzed to construct a probability density function (PDF), which was then converted into a volumetric mass source term for the subsequent molten pool calculation.

First, upon reaching a statistically stationary state of the powder jet, the landing positions of particles on the substrate were sampled. A radial linear probability density function, $P_1(r)$, representing the relative frequency of particles per unit radial length, was derived as:

$$P_1(r)=\frac{N(r)}{\sum N_i\Delta r} \tag{19}$$

where $N(r)$ denotes the number of particles falling within the radial interval at r, and $R_{\max}$ is the maximum radius of the powder spot.

Considering the axisymmetric nature of the annular powder feeding, $P_1(r)$ was normalized to obtain the two-dimensional radial probability distribution function, $P_2(r)$, which characterizes the spatial flux distribution on the substrate surface:

$$P_2(r) = \frac{P_1(r)}{2\pi r} \tag{20}$$

Furthermore, by treating the deposition process as a nozzle scanning over a characteristic plane with velocity v_s, the spatial distribution of the mass input flux, $\dot{m}(r)$, was determined by combining the powder feed rate ($\dot{m}_{feed}$) and powder utilization efficiency η_p:

$$f(r) = \eta_p \dot{m}_{feed} P_2(r) \tag{21}$$

Finally, this distribution function was implemented into the VOF model via a User-Defined Function (UDF) as a mass source term applied to the gas-liquid interface region, thereby achieving one-way coupling from the gas-powder flow to the molten pool dynamics.

3. The Experimental Setup

3.1. Numerical Implementation

3.1.1. Gas-Powder Flow Simulation Setup

To obtain the particle spatial distribution and account for the substrate temperature effect on capture efficiency, a 2D axisymmetric model was constructed for the nozzle region. As shown in **Figure 2(a)**, the computational domain spans a height of 40 mm, with the fluid and solid domains extending to a radius of 10 mm. It includes an upper fluid domain and a lower solid domain (10 mm thick 316L substrate) to simulate the realistic temperature gradient and particle-wall thermal interaction. The grid generation employed a uniform mesh size of 0.025 mm.

The nozzle inlets were set as velocity inlets with a carrier gas velocity of 1 m/s and a shielding gas velocity of 2 m/s. The outer boundaries were defined as pressure outlets. A coupled thermal boundary condition was applied at the fluid-solid interface to enable heat transfer. The DPM approach was used to track particles following a Rosin-Rammler diameter distribution. The powder feed rate was set to 4 g/min.

3.1.2. Molten Pool Dynamics Simulation Setup

A 2D planar VOF model was established to predict the cross-sectional morphology of the clad track. The computational domain **Figure 2(b)** was partitioned into an upper air zone and a lower 316L substrate zone.

A structured quadrilateral mesh was generated with a refined global size of 0.02 mm to capture the air-metal interface. The top boundary was set as a velocity inlet, while the sides were pressure outlets. The bottom and metal sides were treated as walls.

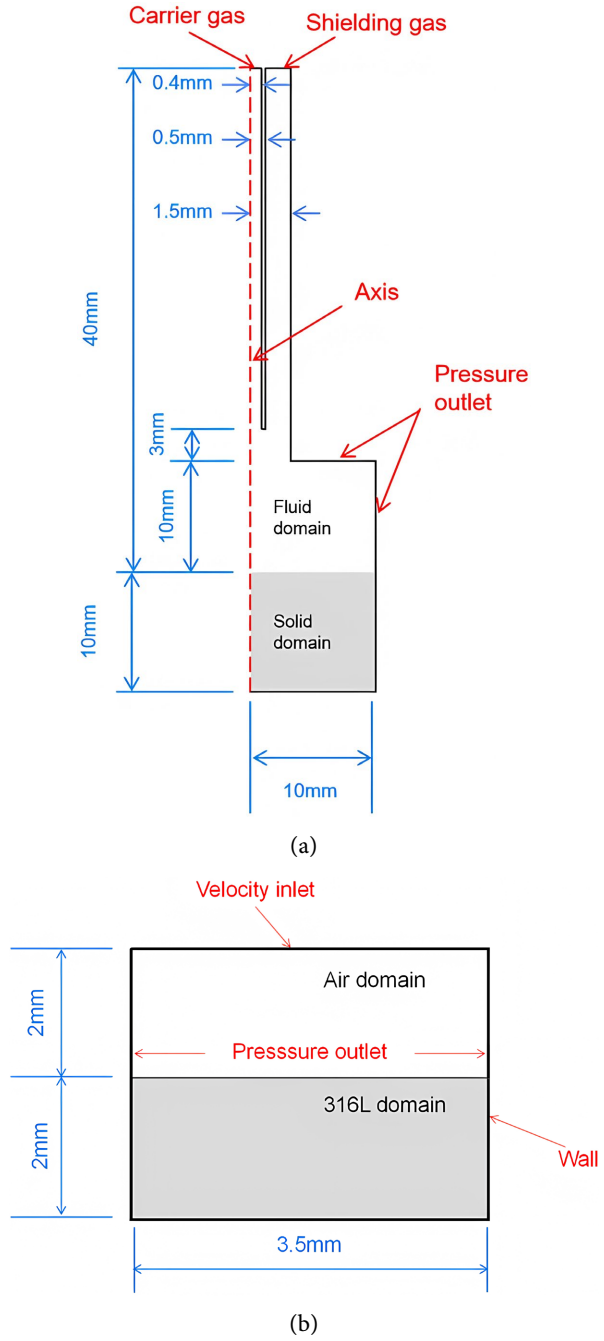

Figure 2. (a) 2D axisymmetric model for gas-powder flow simulation; (b) 2D planar VOF model for molten pool dynamics.

The laser energy and powder mass inputs were implemented via UDFs. Specifically, the annular Gaussian volumetric heat source (Equation (18)) was applied to the mixture phase to generate the local melting pool and drive thermal expansion. Simultaneously, the mass source term, derived from the statistics in Section 3.1.1 (Equation (21)), was applied exclusively to the metal phase continuity equation via a UDF. To prevent non-physical pressurization of the gas phase, an interface-tracking gate was implemented to activate the source term strictly in cells

where the metal volume fraction satisfied $0.5 < \alpha < 1$. This criterion ensures that mass is injected only into the liquid-dominated side of the interface. By avoiding mass addition in gas-dominated cells ($\alpha < 0.5$), the formulation prevents the solver from interpreting the added mass as a compressibility source in the light air phase, thereby eliminating artificial pressure spikes. Consequently, the local pressure field adjusts naturally to the liquid volume increase without numerical divergence.

The transient calculation employed a fixed time step of $\Delta t = 1 \times 10^{-4}$ s for a total duration of 0.5 s (5000 steps). The laser and powder sources were active for 0~0.3333 s and 0.0833~0.25 s, respectively, followed by a cooling period. Initialization was performed using the "Region Adaptation" method (Patch) to define the initial air and substrate phases.

3.2. Physical Experimental Setup

The validation experiments were conducted using a LAM-150 V directed energy deposition (DED) system (Latec, China), which integrates a fiber laser, a 3-axis motion control unit, and a coaxial powder feeding system, as schematically illustrated in **Figure 3**. A coaxial nozzle was employed, with high-purity argon serving as both the carrier gas for powder delivery and the shielding gas for melt pool protection. The substrate was a 316L stainless steel plate with dimensions of 100 mm × 100 mm × 10 mm. Prior to deposition, the substrate surface was mechanically polished to ensure uniform surface roughness and consistent wet ability. The powder was dried and preheated at 200˚C to mitigate moisture-induced agglomeration and porosity defects, thereby enhancing the process stability.

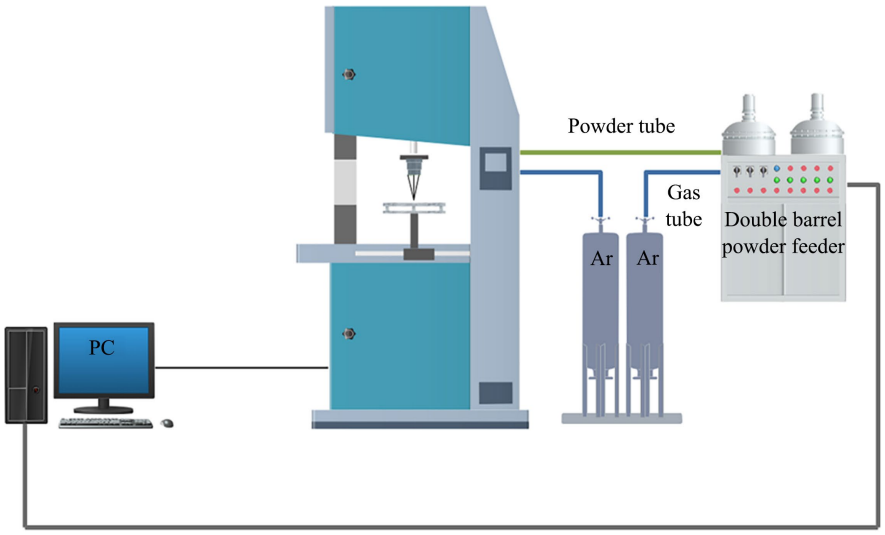

Figure 3. Schematic diagram of the DED experimental setup.

To acquire experimental data for geometric validation, single-track cladding experiments were performed. Two levels of laser power, 500 W and 600 W, were employed to assess the model's accuracy under different thermal inputs, a scan-

ning speed of v_s, and a laser spot diameter of 1 mm. The standoff distance from the nozzle tip to the substrate was maintained at 10 mm. The powder feeding disc rotation speed was set to 2 r/min, corresponding to a mass flow rate of approximately 4 g/min. The detailed processing parameters are listed in Table 2.

Table 2. Processing parameters used in experiment and simulation.

Parameter	Symbol	Value	Unit
Laser power	P	500,600	W
Scanning speed	v_s	4	mm/s
Laser spot outer radius	R_0	0.5	mm
Powder feed rate	$\dot{m}$	4	g/min
Standoff distance	L	10	mm

Upon completion of the deposition, the specimen was sectioned, mounted, ground, and polished according to standard metallographic procedures. The geometric features, specifically the cladding height and width, were measured using an optical microscope .

A critical aspect of the experimental design was the sampling location. The cross-section was extracted at a distance of $z_0 = 1.5$ mm from the starting point. The selection of this position is based on: thermal stability, avoiding the initial transient "break-in period" when the molten pool is not yet stable, to ensure that the measured geometric parameters reflect the quasi-steady-state deposition condition.

4. Results and Discussion

4.1. Gas-Powder Flow Simulation and Effective Capture Analysis

To accurately predict the deposition morphology while maintaining computational efficiency, a sequential one-way coupling strategy was adopted. The specific workflow is designed as follows:

1) First, the carrier gas flow was calculated using the steady RANS equations (as detailed in Section 3) to establish a stable aerodynamic field for particle transport.

2) On the basis of the flow field, a Gaussian heat source was applied to the substrate moving at a scanning speed of v_s. The simulation was run until the laser center reached the position of $z_0 = 1.5$ mm. At this location, the temperature field has stabilized, representing a typical quasi-steady melt pool environment during the cladding process.

3) Finally, the temperature field and flow field were "frozen" at this instant. Powder particles were then injected into this static domain to calculate their trajectories and impact locations.

This approach allows for the precise identification of particle capture behavior under realistic thermal conditions without the excessive computational cost of a fully coupled transient multi-phase simulation.

To determine the effective deposition, a temperature-dependent capture criterion was applied along this radial direction. The local temperature $T(r)$ at each particle's impact location was evaluated against the melting threshold. Particles are considered "effectively captured" only when they impact the region where the substrate temperature exceeds the solidus temperature ($T(r) > T_s$).

As observed in the simulation results, the particle stream is concentrated near the nozzle axis (as shown in Figure 4). However, due to the Gaussian distribution of the heat source, the high-temperature "capture zone" is also centered around the axis. Consequently, particles impacting the peripheral regions, where the substrate remains cold ($T(r) < T_s$), fail to adhere and are treated as rebounding particles. This mechanism effectively filters the incident powder stream, ensuring that only particles interacting with the molten pool contribute to the mass accumulation.

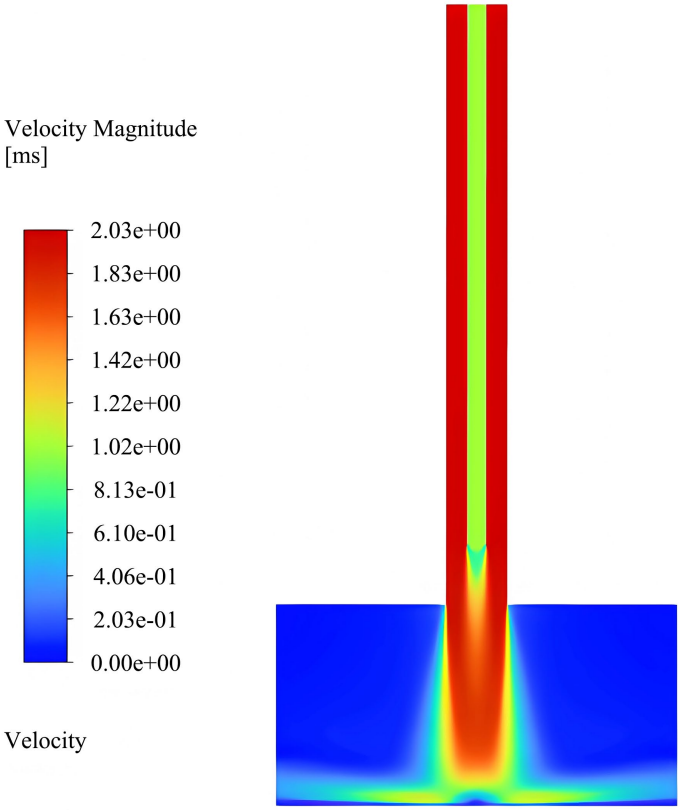

Figure 4. Gas-powder jet velocity field.

Following the particle tracking simulation, the spatial distribution of particles falling into the molten pool was statistically analyzed under different thermal conditions. Figure 5 presents the particle impact frequency distributions along the radial direction for laser powers of 500 W and 600 W, respectively. This frequency distribution is intrinsically based on the effective capture locations, filtering out the rebounding particles and retaining only those that impacted the high-temperature liquid/mushy zone.

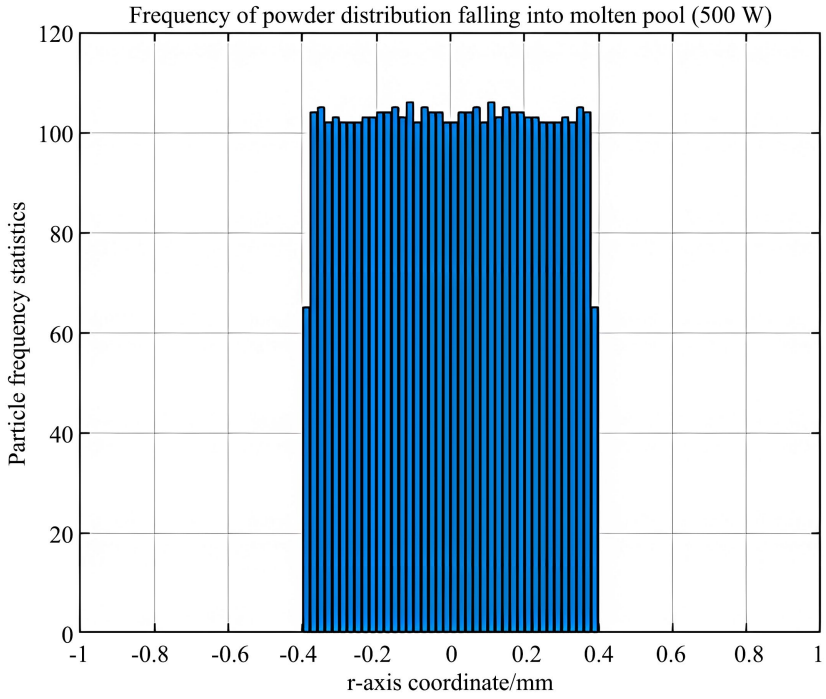

(a)

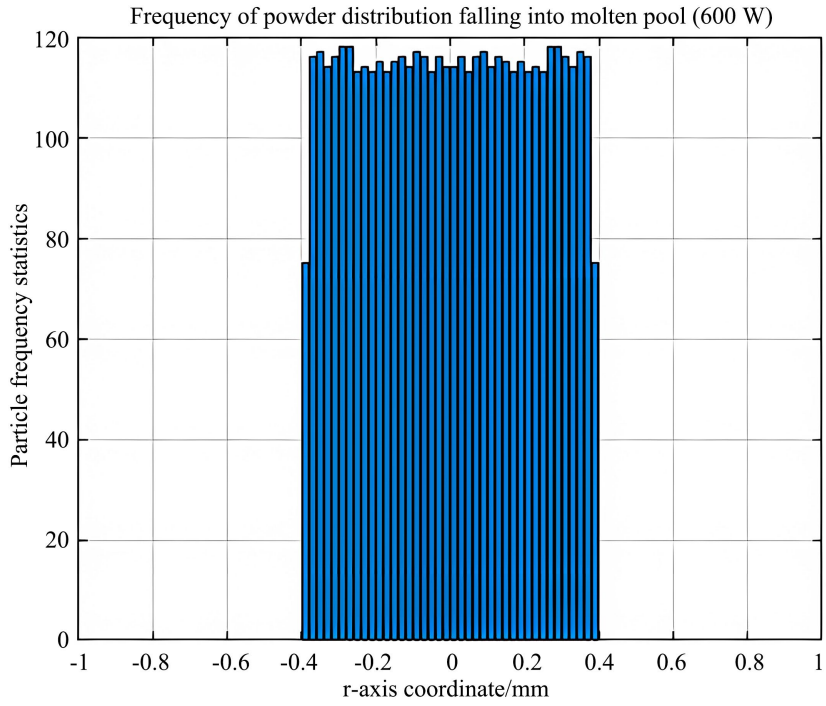

(b)

Figure 5. Frequency of powder distribution falling into the molten pool under different laser powers: (a) 500 W; (b) 600 W.

Crucially, it is observed that for both power levels, the effective particle capture is predominantly concentrated within the radial range of [−0.4, 0.4] mm. This consistency indicates that the spatial profile of the mass source is primarily gov-

erned by the aerodynamic convergence of the powder stream and the central high-temperature region of the laser spot. Although the 600 W case generates a larger molten pool, the effective mass input zone remains constrained within this specific focal area.

To convert the discrete statistical data into a continuous input for the VOF model, the frequency histogram was fitted using a smooth curve. The resulting radial shaping function $f(r)$ (defined in Section 2.2.2) is then used to prescribe the spatial profile of the mass source term in the molten pool simulation, thereby specifying where material is added within the computational domain.

4.2. Molten Pool Dynamics Simulation and Effective Capture Analysis

4.2.1. Bead Morphology and Geometric Validation

To rigorously validate the fidelity of the coupled model, single-track deposition experiments were conducted under two different laser power levels (500 W and 600 W), as outlined in **Table 2.** The simulated molten pool morphology at the steady solidification stage was compared with the experimental metallographic cross-sections.

Figure 6. presents the qualitative comparison of bead morphologies between experimental cross-sections and simulated profiles at laser powers of 500 W (a) and 600 W (b). The VOF model successfully reproduces the characteristic "crescent" shape of the cladding bead, accurately capturing the wetting angle at the edges and the convexity at the crown for both cases.

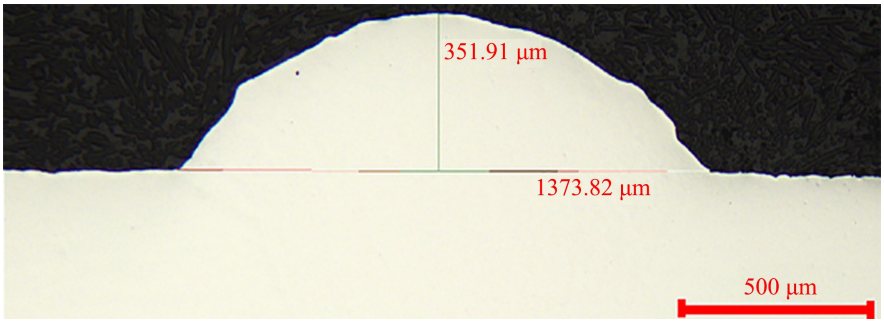

(a)

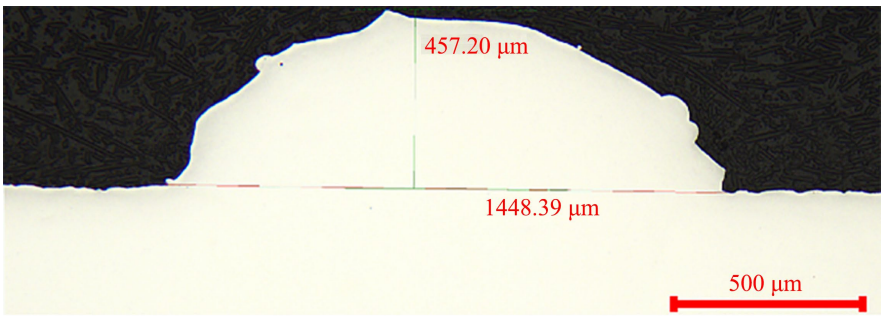

(b)

Figure 6. Experimental bead geometries: (a) 500 W, (b) 600 W.

To explicitly visualize the deposition morphology and extract geometric dimensions, the volume fraction field of the molten pool was analyzed, as illustrated in Figure 7. In the VOF framework, the computational domain consists of two immiscible phases: metal (Phase 1) and gas (Phase 2). During the initialization process, the domain above the substrate was patched as the gas domain (Phase 2 volume fraction set to 1), visualized in blue, while the substrate was defined as the metal domain.

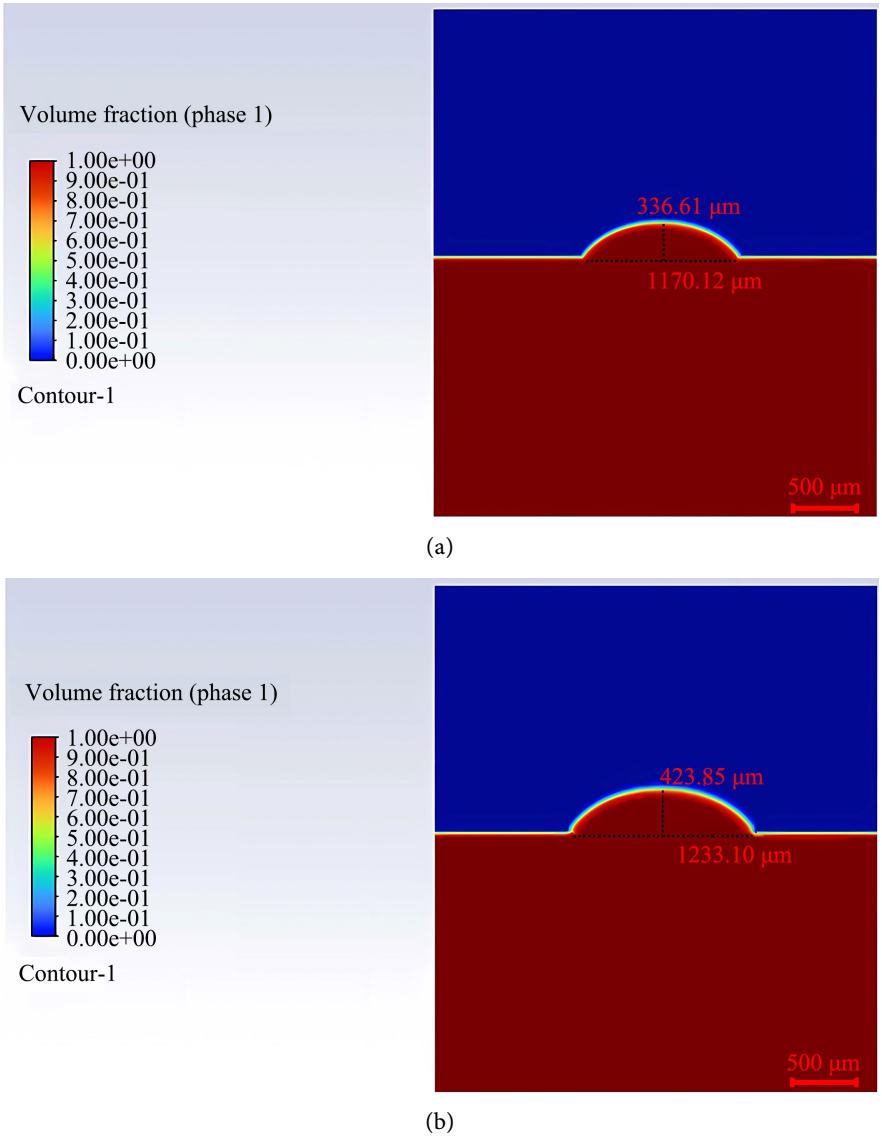

Figure 7. Volume fraction contours of the metal phase in the VOF simulation: (a) 500 W; (b) 600 W.

As powder particles enter the melt pool and fuse, the local volume fraction of Phase 1 increases, expanding the metal domain into the gas region. The final deposited bead is represented by the red region (The metal volume fraction is 1). This sharp phase contrast allows for a clear definition of the gas-metal interface.

Consequently, the cladding height and width were measured by identifying the boundaries where the metal volume fraction transitions from the liquid/solid phase to the gas phase, corresponding to the marked dimensions in **Figure 7(a)** and **Figure 7(b)**.

Quantitatively, the bead height and width were measured to assess the predictive accuracy.

At a laser power of 500 W: The experimentally measured bead height and width were 351.91 μm and 1373.82 μm, respectively. The simulation predicted a height of 336.61 μm and a width of 1170.12 μm. Consequently, the relative error is 4.35% for the height and 14.83% for the width.

At a laser power of 600 W: With the increased energy input, the experimental dimensions expanded to a height of 457.20 μm and a width of 1448.39 μm. The simulation correspondingly predicted a height of 423.85 μm and a width of 1233.10 μm. The calculated relative errors are 7.29% for height and 14.86% for width.

The results indicate that the simulated values are consistently slightly lower than the experimental measurements. However, the maximum deviation for the bead height is controlled within 8%, and the width deviation is stable around 15%. This high level of consistency confirms that the VOF model, by explicitly resolving the gas-metal interface evolution driven by the statistical mass source, can precisely reproduce the experimental bead geometry and mass accumulation process across different processing parameters.

4.2.2. Analysis of Discrepancy and Governing Mechanisms

While the model demonstrates high fidelity, the systematic underestimation of bead dimensions (Sim < Exp) can be attributed to the simplifying assumptions in the multi-phase physics:

Underestimation of Width (Spreading Mechanism): The experimental width is consistently larger (The relative error was 14.8%) than the simulated value. This is primarily due to the surface roughness effect. The simulation assumes an ideally smooth substrate surface, whereas the actual polished substrate possesses micro-roughness. Physically, these surface micro-structures induce a capillary wicking effect, where the micro-grooves create an additional capillary driving force that pulls the liquid metal outwards. This phenomenon effectively enhances the wettability and promotes mechanical spreading beyond the hydrodynamic limit of a smooth surface. Additionally, the VOF mesh resolution (0.02 mm) may filter out the microscopic precursor film at the wetting front, leading to a conservative prediction of the spreading width. The width is dominated by the interplay of thermal wetting and Marangoni convection, and the simulation captures the core flow but underestimates the extreme peripheral spreading.

Underestimation of Height (Capture Efficiency): The simulated height is slightly lower because the "capture-rebound" criterion implemented in the UDF is strictly thermodynamic. In the simulation, particles impacting regions slightly below the capture threshold (e.g., the semi-solid mushy zone boundary) are

treated as rebounding. In the physical experiment, partially melted particles or solid particles can adhere to the sticky semi-solid surface through mechanical interlocking or sintering, contributing to additional height. The model's strict filtration of these "cold" particles leads to a slightly lower calculated mass deposition.

Despite these minor deviations, the model captures the primary physical mechanisms—gas-powder interaction and melt pool thermo-fluid dynamics—making it a reliable tool for process prediction.

5. Conclusions

In this study, a high-fidelity coupled numerical model was developed to investigate the complex multi-physics interactions in Directed Energy Deposition (DED). By integrating a Lagrangian discrete phase model (DPM) for gas-powder flow with a Volume of Fluid (VOF) model for molten pool dynamics, the "process-structure" relationship was quantitatively established. The simulation results were validated against single-track 316L stainless steel deposition experiments. The main conclusions are drawn as follows:

1) A physics-driven decoupled simulation strategy was successfully established. By bridging the macro-scale powder transport and mesoscale melt pool evolution through a statistical mapping method, the computational cost was significantly reduced while maintaining high fidelity. The proposed "mass source implementation based on particle statistics" accurately converts discrete particle trajectories into a continuous boundary condition for the VOF model, ensuring mass conservation and strictly defining the material input zone.

2) A temperature-dependent capture criterion revealed the filtration mechanism of the melt pool. The introduction of the Weber number-based criterion, which accounts for the competition between particle inertia and capillary forces, demonstrated that the effective capture zone is significantly narrower than the geometric powder spot. Only particles impacting the high-temperature central region (where surface tension is reduced) are effectively incorporated, while peripheral particles rebound. This finding emphasizes that the "effective mass flux" is thermally regulated rather than purely aerodynamically determined.

3) The discrepancy between powder flux width and bead width was elucidated. Numerical and experimental results confirmed that the final bead width is significantly larger than the effective powder flux width (0.8 mm). This discrepancy indicates that the deposition morphology is governed by a dual-mechanism: the height is dominated by the localized mass accumulation from the captured powder, while the width is primarily controlled by the thermal wetting behavior and Marangoni convection driven by surface tension gradients.

4) The model demonstrates high predictive accuracy for deposit geometry. Quantitative comparisons under different laser powers (500 W and 600 W) show that the relative errors for bead height are controlled within 4.35% - 7.29%, and the width error is consistent at approximately 14.8%. Although the simulation slightly underestimates the dimensions due to the strict capture criterion and ideal

surface assumptions, the exceptional goodness-of-fit validates the effectiveness of the proposed coupled modeling strategy.

Acknowledgements

This work is supported by the National Natural Science Foundation of China (Grant No.52235006), the Deep Earth probe and Mineral Resources Exploration-National Science and Technology Major Project (Grant No.2024ZD1000800).

Conflicts of Interest

The authors declare no conflicts of interest regarding the publication of this paper.

References

[1] Wang, F., *et al.* (2021) A Review on the Directed Energy Deposition (DED) Technique for Additive Manufacturing: Materials, Processes, and Design. *International Journal of Advanced Manufacturing Technology*, **113**, 1-28.

[2] Carroll, B.E., Otis, R.A., Borgonia, J.P., Suh, J., Dillon, R.P., Shapiro, A.A., *et al.* (2016) Functionally Graded Material of 304L Stainless Steel and Inconel 625 Fabricated by Directed Energy Deposition: Characterization and Thermodynamic Modeling. *Acta Materialia*, **108**, 46-54. https://doi.org/10.1016/j.actamat.2016.02.019

[3] King, W.E., Anderson, A.T., Ferencz, R.M., Hodge, N.E., Kamath, C., Khairallah, S.A., *et al.* (2015) Laser Powder Bed Fusion Additive Manufacturing of Metals; Physics, Computational, and Materials Challenges. *Applied Physics Reviews*, **2**, Article ID: 041304. https://doi.org/10.1063/1.4937809

[4] Thompson, S.M., Bian, L., Shamsaei, N. and Yadollahi, A. (2015) An Overview of Direct Laser Deposition for Additive Manufacturing; Part I: Transport Phenomena, Modeling and Diagnostics. *Additive Manufacturing*, **8**, 36-62. https://doi.org/10.1016/j.addma.2015.07.001

[5] Panwisawas, C., Qiu, C.L., Sovani, Y., Brooks, J.W., Attallah, M.M. and Basoalto, H.C. (2015) On the Role of Thermal Fluid Dynamics into the Evolution of Porosity during Selective Laser Melting. *Scripta Materialia*, **105**, 14-17. https://doi.org/10.1016/j.scriptamat.2015.04.016

[6] Liu, H., Qin, R., Lei, M. and Shi, Y. (2021) Investigation into the Effect of Process Parameters on Powder Flow Characteristics and Melting Behavior in Laser Directed Energy Deposition. *Powder Technology*, **381**, 538-549.

[7] Marchais, K., Girardot, J., Metton, C. and Iordanoff, I. (2021) A 3D DEM Simulation to Study the Influence of Material and Process Parameters on Spreading of Metallic Powder in Additive Manufacturing. *Computational Particle Mechanics*, **8**, 943-953. https://doi.org/10.1007/s40571-020-00380-z

[8] Nan, W. and Ghadiri, M. (2019) Numerical Simulation of Powder Flow during Spreading in Additive Manufacturing. *Powder Technology*, **342**, 801-807. https://doi.org/10.1016/j.powtec.2018.10.056

[9] Kim, J., Ji, S., Yun, Y. and Yeo, J. (2018) A Review: Melt Pool Analysis for Selective Laser Melting with Continuous Wave and Pulse Width Modulated Lasers. *Applied Science and Convergence Technology*, **27**, 113-119. https://doi.org/10.5757/asct.2018.27.6.113

[10] Li, E., Zhou, Z., Wang, L., Zou, R. and Yu, A. (2022) Particle Scale Modelling of Pow-

der Recoating and Melt Pool Dynamics in Laser Powder Bed Fusion Additive Manufacturing: A Review. *Powder Technology*, **409**, Article ID: 117789. https://doi.org/10.1016/j.powtec.2022.117789

[11] Zhang, Y., Wu, S., Guo, Z., Peng, G., Wang, L. and Yan, W. (2025) Defects Caused by Powder Spattering and Entrainment in Laser Powder Bed Fusion Process: High-Fidelity Modeling of Gas, Melt Pool and Powder Dynamics. *Acta Materialia*, **288**, Article ID: 120816. https://doi.org/10.1016/j.actamat.2025.120816

[12] Li, W., Yang, Y. and Zhou, F. (2025) Research on Formation Mechanism of Laser Cladding Micro-Melt Pool Based on Multi-Model Coupling Simulation Technology. *Journal of Materials Engineering and Performance*, **34**, 20683-20699. https://doi.org/10.1007/s11665-025-10792-8

[13] Weisz-Patrault, D. (2020) Fast Simulation of Temperature and Phase Transitions in Directed Energy Deposition Additive Manufacturing. *Additive Manufacturing*, **31**, Article ID: 100990. https://doi.org/10.1016/j.addma.2019.100990

[14] Wang, Z., Liu, M., Luo, Z. and Yan, Z. (2023) Simultaneous Modeling of Powder Rigid Motion and Molten Pool Evolution for Powder-Based Additive Manufacturing. *Powder Technology*, **415**, Article ID: 118118. https://doi.org/10.1016/j.powtec.2022.118118

[15] Wong, S.J.L., Chen, C., Zhi'En, E.T., Raghavan, S. and Li, H. (2025) Novel Interface Model for Integration of Molten Powder Distributive Properties into Multiphase Simulation of Directed Energy Deposition. *International Journal of Thermal Sciences*, **212**, Article ID: 109789. https://doi.org/10.1016/j.ijthermalsci.2025.109789

[16] Ding, Z., Wang, C., Li, H. and Li, Y. (2023) Modeling of Powder Flow and Melt Pool Evolution in Directed Energy Deposition Additive Manufacturing: A Review. *Additive Manufacturing*, **68**, Article ID: 103525.

[17] Menter, F.R. (1994) Two-Equation Eddy-Viscosity Turbulence Models for Engineering Applications. *AIAA Journal*, **32**, 1598-1605. https://doi.org/10.2514/3.12149

[18] Morsi, S.A. and Alexander, A.J. (1972) An Investigation of Particle Trajectories in Two-Phase Flow Systems. *Journal of Fluid Mechanics*, **55**, 193-208. https://doi.org/10.1017/s0022112072001806

[19] Ranz, W.E. and Marshall, W.R. (1952) Evaporation from Drops. *Chemical Engineering Progress*, **48**, 141-146.

[20] Incropera, F.P., DeWitt, D.P., Bergman, T.L. and Lavine, A.S. (2007) Fundamentals of Heat and Mass Transfer. 6th Editon, John Wiley & Sons.

[21] Khairallah, S.A., Anderson, A.T., Rubenchik, A. and King, W.E. (2016) Laser Powder-Bed Fusion Additive Manufacturing: Physics of Complex Melt Flow and Formation Mechanisms of Pores, Spatter, and Denudation Zones. *Acta Materialia*, **108**, 36-45. https://doi.org/10.1016/j.actamat.2016.02.014

[22] Hirt, C.W. and Nichols, B.D. (1981) Volume of Fluid (VOF) Method for the Dynamics of Free Boundaries. *Journal of Computational Physics*, **39**, 201-225. https://doi.org/10.1016/0021-9991(81)90145-5

[23] Voller, V.R. and Prakash, C. (1987) A Fixed Grid Numerical Modelling Methodology for Convection-Diffusion Mushy Region Phase-Change Problems. *International Journal of Heat and Mass Transfer*, **30**, 1709-1719. https://doi.org/10.1016/0017-9310(87)90317-6

[24] Li, Z., Ding, C., *et al.* (2020) Modeling of Annular Laser Beam Powder Feeding Additive Manufacturing. *Additive Manufacturing*, **35**, Article ID: 101370.